CRYSTAL GROWTH & DESIGN

Article

Cite This: Cryst. Growth Des. 2019, 19, 4810−4821

pubs.acs.org/crystal

What Is the Nature of Interactions of BF_4^-, NO_3^-, and ClO_4^- to Cu(II) Complexes with Girard's T Hydrazine? When Can Binuclear Complexes Be Formed?

Tanja Keškić,[†] Božidar Čobeljić,[†] Maja Gruden,[†] Katarina Anđelković,[†] Andrej Pevec,[‡] Iztok Turel,[‡] Dušanka Radanović,*[,§] and Matija Zlatar*[,§]

[†]Faculty of Chemistry, University of Belgrade, Studentski trg 12-16, 11000 Belgrade, Serbia

[‡]Faculty of Chemistry and Chemical Technology, University of Ljubljana, Večna pot 113, 1000 Ljubljana, Slovenia

[§]Department of Chemistry, Institute of Chemistry, Technology and Metallurgy, National Institute, University of Belgrade, Njegoševa 12, 11000 Belgrade, Serbia

Supporting Information

ABSTRACT: In solid-state coordination chemistry, the coordination number of a metal center is not always unambiguously determined, as sometimes from the geometrical parameters it is not clear if ligands are directly bound to the central metal ion or they belong to the outer sphere of a complex. The nature of bonding between Cu(II) and weakly coordinated anions BF_4^-, NO_3^-, and ClO_4^- is investigated by the combined crystallographic and computational study. It is shown that the synergy between the crystal structure determination and computational chemistry allows identification of all interactions present in crystals. Three new complexes, [Cu**L**Cl]BF_4 (**1**), [Cu**L**Cl]NO_3 (**2**), and $[Cu_2\mathbf{L}_2Cl_2](BF_4)_2$ (**3**) with the same [Cu**L**Cl]$^+$ moiety (**L** = (*E*)-*N*,*N*,*N*-trimethyl-2-oxo-2-(2-(1-(pyridin-2-yl)ethylidene)hydrazinyl)ethan-1-amin), were synthesized and characterized by single crystal X-ray diffraction methods and compared to the previously reported [Cu**L**Cl]ClO_4 (**4**). Energy decomposition analysis, noncovalent interaction index analysis, independent gradient model, and the quantum theory of atoms in molecules are performed on the X-ray structures of these four complexes. The results revealed that in **1**, **2**, and **4**, BF_4^-, NO_3^-, and ClO_4^- are weakly, but directly coordinated to the Cu(II) with bonds having high electrostatic character. In **3**, BF_4^- is the counter-anion, electrostatically bonded to the **L**. Furthermore, the present analysis rationalized the fact that only complex **3** is binuclear with bridging Cl^- ions.

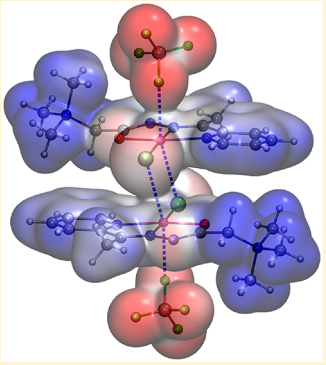

1. INTRODUCTION

Design of molecular crystals requires an explicit understanding of different intra- and intermolecular interactions. Combination of crystal structure determination and computational chemistry emerges as a powerful strategy for the advancement in crystal engineering. Notably, the application of computational chemistry tools allows precise determination of various interactions present in crystals, that surpasses the simple geometrical criteria that are frequently used. In solid-state coordination chemistry, the coordination number of a metal center is typically specified based only on the distance of surrounding ligands to the metal cation. Often this assumption is appropriate. However, in the case of weakly coordinated anions, like tetrafluoroborate (BF_4^-), nitrate (NO_3^-), or perchlorate (ClO_4^-), there is uncertainty whether in crystals they are directly bound to the central metal ion or they belong to the outer sphere of a complex.[1,2] If the central metal ion is Cu(II), the description of coordination geometries is particularly challenging. Complexes of Cu(II) are typically subject to the Jahn−Teller types of distortions resulting in long axial or apical metal−ligand contacts.[3,4] Considering tetragonal Cu(II) complexes, with one or two axial ligands with F, O, or N donor atoms, it is assumed that the ligand is bonded to Cu(II) if the Cu(II)−ligand distance is less than 2.4 Å.[3] If the Cu(II)−ligand distance is larger than 2.8 Å, it is assumed that the Cu(II)−ligand interaction is of the van der Waals type.[3] In the range 2.4−2.8 Å, the ligand should be bonded electrostatically.[3] In the case of chloride ligand, Cl^- is considered bonded if the Cu(II)−Cl distance is less than 2.8 Å and electrostatically bonded if the distance is between 2.8 and 3.2 Å.[3] The three types of Cu(II)−ligand interactions are referred to by Halcrow as genuine, secondary, and van der Waals contacts.[3] This distinction between Cu(II)−ligand interactions is based solely on the sum of corresponding radii.

In this Article, we address the vagueness of the coordination of BF_4^-, NO_3^-, and ClO_4^- to Cu(II) by a combined crystallographic and computational study. For this study, three new complexes, [Cu**L**Cl]BF_4 (**1**), [Cu**L**Cl]NO_3 (**2**), and $[Cu_2\mathbf{L}_2Cl_2](BF_4)_2$ (**3**), with the same [Cu**L**Cl]$^+$ fragment (**L** = (*E*)-*N*,*N*,*N*-trimethyl-2-oxo-2-(2-(1-(pyridin-2-yl)ethylidene)-

Received: June 13, 2019
Revised: July 5, 2019
Published: July 15, 2019

DOI: 10.1021/acs.cgd.9b00760
Cryst. Growth Des. 2019, 19, 4810−4821

hydrazinyl)ethan-1-amin) were synthesized and characterized by single crystal X-ray diffraction methods and compared to the previously reported [CuLCl]ClO_4 (**4**).[5] The structures of newly synthesized complexes **1**−**3**, as well as the structure of **4**,[5] are perfect examples of the intricate bonding present in crystals of Cu(II) complexes. Density functional theory (DFT) based analysis of the X-ray structures of these four complexes containing the same inner-sphere cation and different anions is performed to understand the nature of bonding between Cu(II) and weakly coordinated anions. Namely, energy decomposition analysis,[6−8] noncovalent interaction (NCI) index analysis,[9] independent gradient model (IGM),[10,11] and the quantum theory of atoms in molecules (QTAIM)[12] are used to identify all interactions present in the crystals of these complexes. This analysis helps in understanding the coordination geometry around the Cu(II) ion in crystals. Also, this study discerns whether the self-assemblies of the complexes, as found in the crystals, are de facto polynuclear complexes.

2. EXPERIMENTAL SECTION

2.1. Materials and Methods. 2-Acetylpyridine (≥99%) and Girard's T reagent (99%) were obtained from Aldrich. IR spectra were recorded on a Nicolet 6700 FT-IR spectrometer using the ATR technique in the region 4000−400 cm^{-1} (s-strong, m-medium, w-weak). Elemental analyses (C, H, and N) were performed by standard micromethods using the ELEMENTARVario ELIII C.H.N.S.O analyzer.

2.2. Synthesis. *2.2.1. Synthesis of Ligand HLCl (E)-N,N,N-trimethyl-2-oxo-2-(2-(1-(pyridin-2-yl)ethylidene)hydrazinyl)ethan-1-aminium-chloride.* The ligand **HL**Cl was synthesized by the reaction of Girard's T reagent (1.676 g, 1.00 mmol) and 2-acetylpyridine (1.120 mL, 1.00 mmol) in methanol (50 mL). The reaction mixture was acidified with 3−4 drops of 2 M HCl and was refluxed for 2 h at 85 °C. IR (cm^{-1}): 3387 (w), 3127 (m), 3090 (m), 3049 (m), 3016 (m), 2950 (s), 1700 (vs), 1612 (w), 1549 (s), 1485 (m), 1400 (m), 1300 (w), 1253 (w), 1200 (s), 1153 (w), 1135 (m), 1095 (w), 1073 (m), 975 (w), 944 (w), 914 (m), 748 (w), 683 (w). Elemental analysis calcd for $C_{12}H_{19}ClN_4O$: C 53.23%, H 7.07%, N 20.69%, found: C 53.42%, H 7.12%, N 20.77%.

2.2.2. Synthesis of [CuLCl]BF_4 (1) and [$Cu_2L_2Cl_2$](BF_4)$_2$ (3). The mononuclear (**1**) and binuclear (**3**) Cu(II) complexes were synthesized by the reaction of $Cu(BF_4)_2{\cdot}6H_2O$ (0.115 g, 0.30 mmol) and ligand **HL**Cl (0.081 g, 0.30 mmol) in methanol (20 mL). The solution was refluxed for 4 h. After slow evaporation of the solvent in the refrigerator (∼7 °C) for 10 days, two kinds of green crystals suitable for X-ray analysis were formed. The main fraction corresponds to compound **1**, while complex **3** was obtained only in traces.

2.2.3. Synthesis of [CuLCl]NO_3 (2). Into a methanol solution (10 mL) of ligand **HL**Cl (0.054 g, 0.20 mmol), $Cu(NO_3)_2{\cdot}3H_2O$ (0.050 g, 0.20 mmol) dissolved in 5 mL of methanol was added. The reaction mixture was refluxed for 4 h. After refrigeration of the reaction solution at −8 °C for a 1 week, green crystals suitable for X-ray analysis were formed. Yield: 72 mg (91%). IR (cm^{-1}): 3373 (vs), 3326 (m), 3271 (vs), 3106 (m), 3061 (m), 3031 (m), 1596 (vs), 1561 (m), 1529 (w), 1482 (s), 1443 (s), 1365 (m), 1307 (m), 1265 (w), 1196 (w), 1167 (m), 1118 (w), 1075 (w), 1048 (w), 1021 (w), 981 (w), 909 (w), 784 (s), 675 (w), 648 (w), 575 (w). Elemental analysis calcd for $C_{12}H_{18}ClCuN_5O_4$: C 36.46%, H 4.59%, N 17.72%, found: C 36.57%, H 4.64%, N 17.48%.

2.3. X-ray Crystallography. The molecular structures of complexes **1**, **2**, and **3** were determined by single crystal X-ray diffraction methods. Crystallographic data and refinement details are given in Supporting Information (SI). Diffraction data for **1**−**3** were collected at 150 K for **1** and **3** and 293 K for **2** with Agilent SuperNova dual source diffractometer using an Atlas detector and equipped with mirror-monochromated Mo Kα radiation (λ = 0.71073 Å). The data were processed by using CrysAlis PRO.[13] All the structures were solved using SIR-92[14] (**1** and **3**) or SHELXS-97[15] (**2**) and refined against F^2 on all data by full-matrix least-squares with SHELXL-2016.[16] All non-hydrogen atoms were refined anisotropically. All other hydrogen atoms were included in the model at geometrically calculated positions and refined using a riding model. The *ORTEP-3*[17] for Windows and *MERCURY*[18] programs were used for graphical presentations. CCDC 1917721 (for **1**), 1917722 (for **2**), and 1917723 (for **3**) contain the supplementary crystallographic data for this paper. These data can be obtained free of charge from The Cambridge Crystallographic Data Centre via www.ccdc.cam.ac.uk/data_request/cif.

2.4. Computational Details. All calculations were performed using DFT formalism on the model systems constructed from the corresponding crystal structures (structures **1**−**4**). For mononuclear complexes, the interaction between [CuLCl]$^+$ and the nearest counter-anions in the X-ray determined geometries of **1**, **2**, **3**, and **4** structures were studied. To understand the formation of binuclear complexes, the interactions between two monomer units from the X-ray structures were investigated. In the X-ray structures of **1** and **4**, BF_4^- and ClO_4^-, respectively, are disordered. To see how the geometries of anions influence the analysis, constrained geometry optimizations of F atoms in the dimeric structure of **1** and O(perchlorate) atoms in the dimeric structure of **4** have been performed with the ORCA 4.1.1 program,[19,20] using the revPBE[21] exchange-correlation functional with Grimme's third generation dispersion energy correction[22] and Becke-Johnson damping,[23] i.e., the revPBE-D3 functional. Relativistic effects were accounted for by Zeroth-Order Regular Approximation (ZORA) in in the scalar-relativistic formulation.[24−26] ZORA-def2-TZVP basis set for all atoms and the resolution-of-the-identity approximation in the Split-RI-J variant and the scalar relativistically recontracted SARC/J Coulomb fitting sets were used.[27−29]

The nature of the interaction between chosen fragments was analyzed with the aid of the extended transition state energy decomposition scheme (EDA)[6−8] as implemented in ADF program package.[30−32] The interaction energy between fragments is decomposed into four chemically meaningful components: $E_{int} = E_{elst} + E_{Pauli} + E_{orb} + E_{disp}$. The term E_{elst} is the quasi-classical electrostatic interaction between the fragments; E_{Pauli} is the repulsive Pauli interaction between occupied orbitals on the two fragments and accounts for a steric interaction; E_{orb} is a stabilizing contribution due to the charge transfer and polarization; E_{disp} is the dispersion energy correction. Additionally, natural orbitals for chemical valence (NOCV)[33,34] decomposition of the electron density deformation was performed to elucidate different density transfer channels and to quantify their importance as an energy contribution to the E_{orb}. Charge flow between the fragments was quantified with Hirshfeld charge analysis.[35] For energies, the general gradient approximations (GGA) in the forms of BP86,[36−38] PBE,[39] and revPBE[21] were used, with Grimme's third generation dispersion energy correction[22] and Becke−Johnson damping,[23] i.e., BP86-D3, PBE-D3, and revPBE-D3 functionals. Furthermore, the dispersion corrected meta-GGA, M06L[40,41] functional with zero damping (parameters: s_6 = 1.0, $s_{r,6}$ = 1.325, s_8 = 0.0) was used. ZORA in the scalar-relativistic formulation[24,25] has been used. An all-electron triple-ζ Slater-type orbitals plus one polarization function (TZP) basis set was employed for all atoms.

Noncovalent interactions between fragments had been identified with the aid of the Non-Covalent Interactions Index (NCI)[9] and Independent Gradient Model (IGM)[10,11] methods. Interactions between fragments were also analyzed within the framework of Bader's Quantum Theory of Atoms in Molecules (QTAIM).[12] NCI, IGM, and QTAIM analyses were performed by Multiwfn software v 3.6[42] on the wave functions generated at the self-consistent (SC) revPBE-NL/ZORA-def2-TZVP level of theory. revPBE-NL[43] is the nonlocal (NL) density-dependent dispersion functional.[44] DFT-NL calculations were carried out with the ORCA 4.1.1 program[19,20] with the resolution-of-the-identity approximation in the Split-RI-J variant and the scalar relativistically recontracted SARC/J Coulomb fitting sets.[27−29] The NCI model is based on the visualization of the

DOI: 10.1021/acs.cgd.9b00760
Cryst. Growth Des. 2019, 19, 4810−4821

isosurfaces of the reduced density gradient(s) colored by the product of the sign of the second eigenvalue of the electron density Hessian and the electron density ($\mathrm{sign}(\lambda_2) \times \rho$). Isosurfaces are colored with the "Blue-Green-Red" color scheme, so that the strong attractive interactions (negative $\mathrm{sign}(\lambda_2) \times \rho$) are blue, weak attractive interactions and van der Waals interactions are green ($\mathrm{sign}(\lambda_2) \times \rho$ close to zero), and steric repulsion is red (positive $\mathrm{sign}(\lambda_2) \times \rho$). Localized interactions are disk-shaped, while delocalized interactions are depicted as diffused surfaces. Thus, the shape and color of the isosurfaces are informative of the type and spatial localization of the noncovalent interactions. The IGM model is based on calculating $\delta g = g^{\mathrm{IGM}} - g$, where g^{IGM} is the density gradient calculated as the sum of the absolute value of the density gradient of each atom in their free-states and g is the true density gradient. In the IGM model, δg can be defined only in the interfragment region, and isosurfaces of $\delta g^{\mathrm{inter}}$ colored by the $\mathrm{sign}(\lambda_2) \times \rho$ are used to identify various interfragment interactions analogously to the NCI method. IGM isosurfaces are more rounded in shape compared to the NCI isosurfaces. QTAIM is based on the topological analysis of the electron density. The electron density, its Laplacian, the total energy density, the potential energy density, and the kinetic energy density at interfragment bond critical points were used for additional study of chemical bonding between fragments.

3. RESULTS AND DISCUSSION

3.1. General. The ligand, (*E*)-*N*,*N*,*N*-trimethyl-2-oxo-2-(2-(1-(pyridin-2-yl)ethylidene)hydrazinyl)ethan-1-aminium-chloride (**HL**Cl), was obtained from the condensation reaction of 2-acetylpyridine and Girard's T reagent in methanol (Scheme 1). In the reaction of ligand **HL**Cl with $Cu(BF_4)_2 \cdot 6H_2O$ in a 1:1 molar ratio in methanol, a mixture of mononuclear (**1**) and binuclear (**3**) Cu(II) complexes was obtained (Scheme 1). Changing the polarity of the solution using a different solvent or mixture of solvents, as well as changing the molar ratio of reactants, did not affect the results obtained (additional experimental details are in SI). The reaction of **HL**Cl with $Cu(NO_3)_3 \cdot 3H_2O$ in a 1:1 molar ratio, in methanol, gives mononuclear Cu(II) complex **2**, with composition [Cu**L**Cl]NO_3 (Scheme 1).

Scheme 1. Schematic Presentation of the Synthesis of Ligand (HLCl) and Complexes 1, 2, and 3

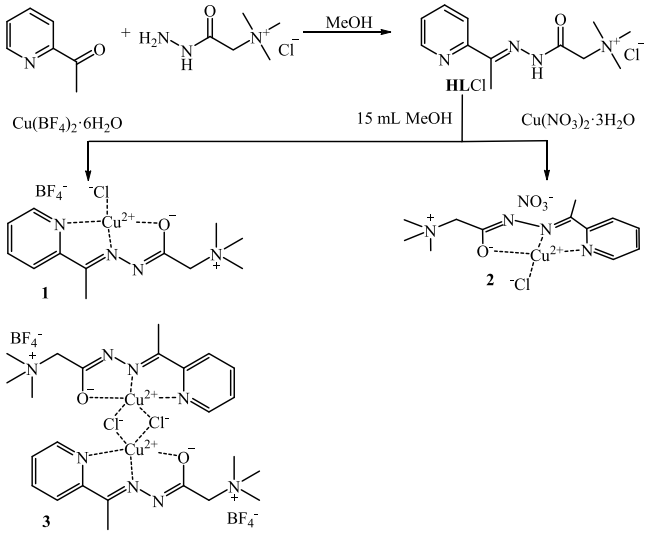

The ligand **HL**Cl has recently been used for the preparation of mononuclear [Cu**L**Cl]ClO_4 (**4**) and binuclear $[Cu_2\mathbf{L}_2(\mu_{-1,1}\text{-}N_3)_2](ClO_4)_2$ complexes.[5] Both complexes were found to be good catalysts in the synthesis of *N*-arylatedimidazoles and benzimidazoles.[5] The **HL**Cl ligand possesses a positively charged quaternary ammonium fragment and can exist either in protonated monocationic form or as a deprotonated zwitterionic ligand. In mononuclear complex **4** and binuclear $[Cu_2\mathbf{L}_2(\mu_{-1,1}\text{-}N_3)_2](ClO_4)_2$ complex, the hydrazone based ligand is zwitterionic and the distorted square-planar and square-pyramidal geometries of Cu(II) ions, respectively, have been established by X-ray crystallography. However, if long Cu···O(perchlorate) contacts are considered as weak coordinative bonds, Cu(II) in **4** is a distorted square-pyramid, while in $[Cu_2\mathbf{L}_2(\mu_{-1,1}\text{-}N_3)_2](ClO_4)_2$ it is of pseudo-octahedral geometry. Furthermore, in the crystals of mononuclear complex **4**, complex cations $[Cu\mathbf{L}Cl]^+$ of square-planar geometry are linked through in-plane coordinated chloride anions so to mimic a dimeric structure $[Cu_2\mathbf{L}_2Cl_2](ClO_4)_2$ with the distance of approximately 3.6 Å between the Cu(II) centers.[5] Considering the crystal structures of related mononuclear Cu(II) complexes, we have found relatively short Cu(II)···Cu(II) separations, nearly 4.0 Å, in two structures $[Cu(\mathbf{HL}^2)Cl_2Cu\mathbf{HL}^2Cl(H_2O)]Cl$ ($\mathbf{HL}^2$ = 2-formylpyridine semicarbazone)[45] and $[Cu\mathbf{HL}^4Cl_2]$ ($\mathbf{HL}^4$ = 2-pyridine-carboxaldehyde 4-dimethylaminobenzoylhydrazone).[46] However, in the other mononuclear Cu(II) considered, the distance between the closest metal centers exceeds 6.4 Å (vide infra).[47−49] Cu(II) ions in the herein reported structures **1** and **2** are either in a distorted square-planar or a distorted square-pyramidal environment. The coordination geometry of **1** and **2** depends on whether BF_4^- and NO_3^- are considered as counter-anions, or they are coordinated to the Cu(II). Both **1** and **2**, similarly to **4**, can be considered as dimeric structures linked through in-plane coordinated chloride anions with the distance between the closest Cu(II) centers of approximately 3.6 and 3.8 Å, respectively. In binuclear complex **3**, BF_4^- is not bonded to Cu(II) but is linked via hydrogen bonds to the **L** (vide infra). In the binuclear complexes $[Cu_2L_2(\mu_{-1,1}\text{-}N_3)_2](ClO_4)_2$ and **3**, the distance between the closest Cu(II) centers is approximately 3.4 Å.

3.2. Crystal Structures of $[Cu\mathbf{L}Cl]BF_4$ (1), $[Cu\mathbf{L}Cl]NO_3$ (2), and $[Cu_2\mathbf{L}_2Cl_2](BF_4)_2$ (3) Complexes. The molecular structures of $[Cu\mathbf{L}Cl]BF_4$ (**1**), $[Cu\mathbf{L}Cl]NO_3$ (**2**), and $[Cu_2\mathbf{L}_2Cl_2](BF_4)_2$ (**3**) with atom numbering schemes are presented in Figures 1a, 2, and 3, respectively. The selected bond lengths and bond angles for **1**, **2**, and **3** are given in SI (Table S2). The structural parameters correlating the geometry of related mononuclear[5,45−49] (**1**, **2**, and **4**−**10**) and binuclear[50−52] (**3**, **11**−**14**) Cu(II) complexes with hydrazone-based NNO-donor ligands are listed in Table 1.

Complex **1** crystallizes in the monoclinic centrosymmetric space group $P2_1/c$, with the asymmetric unit comprising one complex cation $[Cu\mathbf{L}Cl]^+$ and statistically disordered BF_4^- anion. The complexes **1**, **2**, and **4**[5] are isostructural. The complex cation features a four-coordinate Cu(II) center with the NNO donor set of tridentate zwitterionic ligand **L** and the Cl^- ion supplementing the fourth coordination site (Figure 1a). The coordination geometry around Cu(II) may be described as distorted square planar with τ_4 parameter[53] of 0.17 for **1** ($\tau_4 = 360° - (\alpha + \beta)/141°$, where α and β are the two largest angles around the central atom). The values of τ_4 can range from 1.00 for a perfect tetrahedral geometry to zero for a perfect square planar. Intermediate structures, including trigonal pyramidal and seesaw, fall within the range of 0−1.00.

DOI: 10.1021/acs.cgd.9b00760
Cryst. Growth Des. 2019, 19, 4810−4821

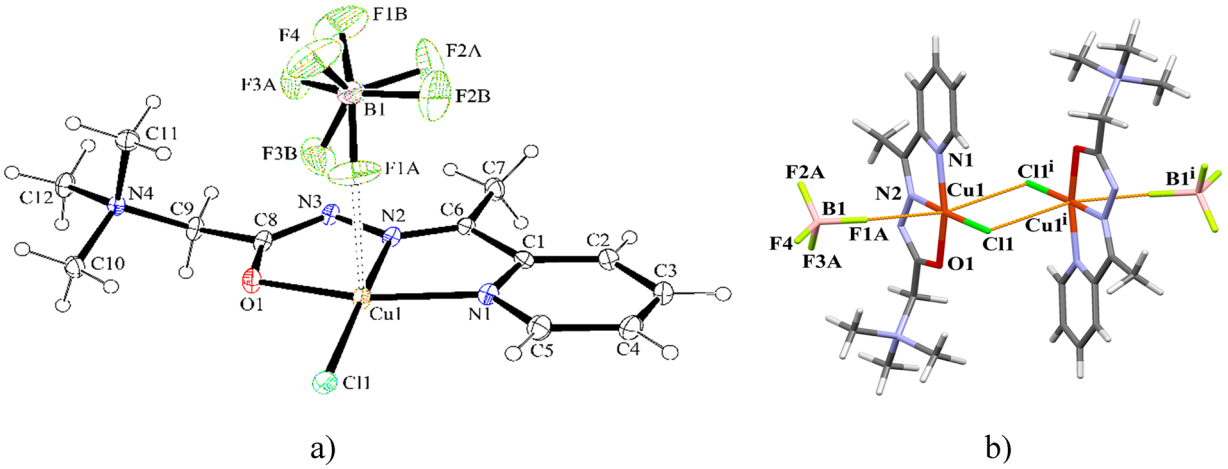

Figure 1. (a) ORTEP presentation of the $[CuLCl]BF_4$ (**1**). Thermal ellipsoids are drawn at the 30% probability level. Long contact Cu···F is represented as a dashed line. (b) View of the dimeric unit of **1** of pseudo-octahedral geometry. Long contacts Cu···F and Cu···Cl are represented as orange lines. BF_4^- anions suffer from positional disorder. Symmetry code i stands for 2-*x*, -*y*, 2-*z*.

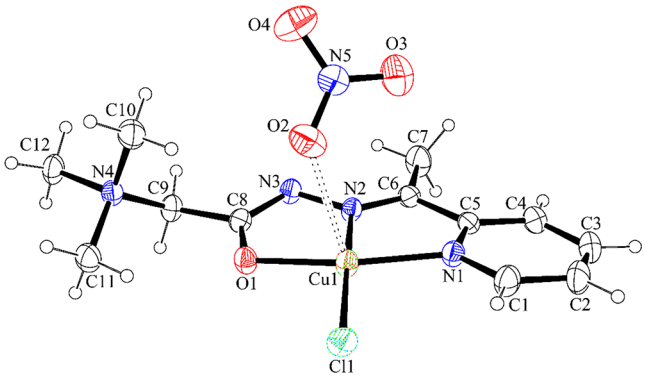

Figure 2. ORTEP presentation of the $[CuLCl]NO_3$ (**2**). Thermal ellipsoids are drawn at the 30% probability level. Long contact Cu···O is represented as a dashed line.

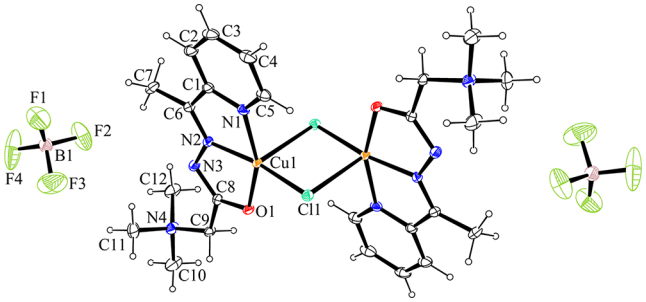

Figure 3. ORTEP presentation of the $[Cu_2L_2Cl_2](BF_4)_2$ (**3**). Thermal ellipsoids are drawn at the 30% probability level. The unlabeled part of the dimeric molecule and one BF4$^-$ counter-anion are generated by symmetry operation -*x*, -*y*, 1-*z*.

The tridentate NNO coordination of **L** to Cu(II) ion generates two five-membered chelate rings (Cu−N−C−C−N and Cu−N−N−C−O) fused along the Cu1−N2 bond. The chelate rings are non-coplanar, as indicated by the dihedral angle of 3.5°. Similarly, as in the case of **4**, the complex units of **1** are organized into $[Cu_2L_2Cl_2](BF_4)_2$ dimers (Figure 1b) in which the symmetry related Cu(II) ions of tetragonally elongated octahedral geometry are separated by 3.5990(4) Å. In the crystals of **1**, the complex molecules are arranged in layers parallel with the (0 0 1) lattice plain by means of intermolecular C−H···F and C−H···Cl hydrogen bonds (cf., SI). The adjacent layers are packed via C7−H7A···F2A and C12−H12C···F3A hydrogen bonds into the three-dimensional supramolecular structure. The Cu−N_{py} (2.0023(19) Å), Cu−N_{imine} (1.9308(18) Å), Cu−O (1.9806(15) Å), and Cu−Cl (2.2141(6) Å) distances are similar to those for copper(II) complexes where the metal ions are coordinated to the same type of atoms (Table 1). As expected, the complexes **6**−**10** show slightly longer Cu−O_{am} (2.035(2)−2.137(2) Å) distances compared to the distances (1.953(3)−1.990(3)Å) observed in complexes **1**−**5** and **11**−**14** having a deprotonated amide-O bound copper(II).

Complex **2** also crystallizes in the monoclinic space group $P2_1/c$. The asymmetric unit of **2** comprises the complex cation $[CuLCl]^+$ and NO_3^- anion (Figure 2). Complexes **1** and **2** show greater distortion from a perfect square planar configuration than complex **4**, as indicated by the calculated τ_4 parameters of 0.17 and 0.19 vs 0.15 (Table 1). Crystal packing of **2** is similar to that of **1** and **4**. In the crystals of **2**, the complex molecules are connected by means of intermolecular C−H···O and C−H···Cl hydrogen bonds into the layer parallel with the (0 0 1) lattice plain (cf., SI). The adjacent layers are packed via C12−H12A···O4 hydrogen bond to form a three-dimensional supramolecular structure. In complexes **1**, **2**, **4**,[5] and **6**[45] the formation of dimeric units $[Cu_2L_2Cl_2](BF_4)_2$, $[Cu_2L_2Cl_2](NO_3)_2$, $[Cu_2L_2Cl_2](ClO_4)_2$, and $[Cu(HL^2)Cl_2CuHL^2Cl(H_2O)]^+$, respectively, is accomplished by linking the metal centers through in-plane coordinated chloride anions which leads to short separations between the closest Cu atoms (Cu···Cu is in the range 3.5793(8)−3.902(1)Å) in comparison to those observed for **5**, **7**, **9**, and **10**. In complex **8**, a relatively short Cu···Cu distance of 4.023(1) Å is achieved by π-stacking of the neighboring hydrogen bonded dimers. The other mononuclear Cu(II) complexes (**5**, **7**, **9**, and **10**) listed in Table 1 show significantly longer Cu···Cu separations.

Complex **3** crystallizes in the monoclinic space group $P2_1/n$, with the asymmetric unit comprising one Cu(II) center, zwitterionic ligand **L**, one Cl^- ion, and BF_4^- counter-anion. The crystal structure displays a centrosymmetric binuclear complex with the crystallographically independent Cu1 center being coordinated to three donor atoms (N1, N2, and O1) of

DOI: 10.1021/acs.cgd.9b00760
Cryst. Growth Des. 2019, 19, 4810−4821

Table 1. Structural Parameters Correlating the Geometry of Related Mono- and Binuclear Cu(II) Complexes with Hydrazone-Based NNO-Donor Ligands[a]

Complexes	CN[b]	Cu—Cu (Å)	Bond lengths (Å)		τ_4/τ_5[c]	ρ[d] (Å)	Cu−Cl−Cu (deg)	ref.
			In-plane	Axial				
Mononuclear								
[CuLCl]BF_4 (**1**)	4	3.5990(4)	Cu1−N1 2.0023(19) Cu1−N2 1.9308(18) Cu1−O1 1.9806(15) Cu1−Cl1 2.2141(6)		0.17			This work
[CuLCl]NO_3 (**2**)	4	3.7973(5)	Cu1−N1 2.0031(18) Cu1−N2 1.9239(18) Cu1−O1 1.9777(15) Cu1−Cl1 2.2056(6)		0.19			This work
[CuLCl]ClO_4 (**4**)	4	3.5793(8)	Cu1−N1 2.005(4) Cu1−N2 1.931(4) Cu1−O1 1.990(3) Cu1−Cl1 2.2175(14)		0.15			5
[CuL^1Cl(DMSO)][e] (**5**)	5	6.5328(5)	Cu−N1 2.043(2) Cu−N2 1.942(2) Cu−O1 1.988(2) Cu−Cl 2.2354(7)	Cu−O2 2.242(2)	0.08	0.2205(3)		47
[Cu(HL^2)Cl_2	5	3.902(1)	Cu1B−N2B 2.022(2)		0.04	0.2329(4)		
$CuHL^2Cl(H_2O)$]Cl[e,g] (**6**)			Cu1B−N1B 1.956(2) Cu1B−O1B 2.035(2) Cu1B−Cl2B 2.2186(12) Cu1A-N2A 2.037(2) Cu1A-N1A 1.948(2) Cu1A-O1A 2.039(2) Cu1A-Cl1A 2.1983(10)	Cu1B−Cl1B 2.5737(9) Cu1A-O2A 2.397(2)	0.27	0.0928(4)		45
[$CuHL^3Cl_2$][f,h] (**7**)	5	7.0803(5)	Cu−N1 2.044(2) Cu−N2 1.971(2) Cu−O1 2.137(2) Cu−Cl2 2.2212(8	Cu−Cl1 2.4344(8)	0.22	0.3292(3)		47
[$CuHL^4Cl_2$][f,i] (**8**)	5	4.023(1)	Cu1−N1 2.044(2) Cu1−N2 1.961(2) Cu1−O1 2.063(2) Cu1−Cl1 2.2053(9)	Cu1−Cl2 2.5128(10)	0.16	0.2753(4)		46
[$CuHL^5Cl_2$][f,j] (**9**)	5	6.650(2)	Cu1−N3 2.031(2) Cu1−N2 1.965(2) Cu1−O1 2.059(2) Cu1−Cl1 2.2110(7)	Cu1−Cl2 2.4892(9)	0.06	0.3553(3)		48
[$CuHL^6Cl_2$][f,k] (**10**)	5	6.447(1)	Cu1−N1 2.0390(16) Cu1−N2 1.9638(15) Cu1−O1 2.0872(14) Cu1−Cl2 2.2116(6)	Cu1−Cl3 2.4655(7)	0.22	0.3018(2)		49
Binuclear								
[$Cu_2L_2Cl_2$]$(BF_4)_2$ (**3**)	5	3.3644(6)	Cu1−N1 2.023(3) Cu1−N2 1.931(3) Cu1−O1 1.977(2) Cu1−Cl1 2.2408(8)	Cu1−$Cl1^{ii}$ 2.6800(9)	0.17	0.1820(4)	85.78(3)	This work
[$Cu_2(L^7)_2(Cl)_2$][l] (**11**)	5	3.4000(3)	Cu1−N1 2.0008(14) Cu1−N2 1.9347(14) Cu1−O1 1.9623(12) Cu1−Cl1 2.2425(4)	Cu1−$Cl1^{iii}$ 2.8033(5)	0.17	0.1034(2)	83.94(2)	50
[$Cu_2(L^8)_2(Cl)_2$][m] (**12**)	5	3.3691(4)	Cu1−N1 2.0084(18) Cu1−N2 1.9374(16) Cu1−O1 1.9636(14) Cu1−Cl1 2.2430(6)	Cu1−$Cl1^{ii}$ 2.7158(6)	0.08	0.1611(3)	85.03(2)	51
[$Cu_2(L^9)_2(Cl)_2$][n] (**13**)	5	3.4085(8)	Cu1−N1 2.017(3) Cu1−N2 1.932(3) Cu1−O1 1.953(3) Cu1−Cl1 2.2572(9)	Cu1−$Cl1^{iv}$ 2.6206(10)	0.02	0.2468(4)	88.33(3)	52

DOI: 10.1021/acs.cgd.9b00760
Cryst. Growth Des. 2019, 19, 4810−4821

Table 1. continued

Complexes	CN[b]	Cu—Cu (Å)	Bond lengths (Å) In-plane	Bond lengths (Å) Axial	τ_4/τ_5[c]	ρ[d] (Å)	Cu−Cl−Cu (deg)	ref.
Binuclear								
$[Cu_2(\mathbf{L}^{10})_2(Cl)_2]$[o] (**14**)	5	3.2926(5)	Cu1−N1 2.0003(17) Cu1−N2 1.9431(18) Cu1−O1 1.9569(15) Cu1−Cl1 2.2523(6)	Cu1−Cl1^{iv}2.6248(6)	0.11	0.1878(3)	84.56(2)	52

[a]Symmetry codes: ii = -*x*, -*y*, -*z* + 1; iii = -*x* + 1, -*y* + 2, -*z* + 1; iv = -*x* + 1, -*y* + 1, -*z*. [b]CN = Coordination number. [c]For Cu(II) complexes of CN = 4, the τ parameter has been calculated using the equation $\tau_4 = 360° - (\alpha + \beta)/141°$, where α and β are the two largest angles around the central atom. For Cu(II) complexes of CN = 5, the τ parameter has been calculated using the equation $\tau_5 = (\beta - \alpha)/60$, where β and α are the two largest angles around the central atom. [d]ρ (Å) is the distance of the metal ion from the mean basal plane of the square pyramid toward the apical ligand. [e]$\mathbf{L}^1$ = 2-formylpyridine-*para*-nitro-phenyl hydrazone. [f]Complexes having keto-O bound copper(II). [g]$\mathbf{HL}^2$ = 2-formylpyridine semicarbazone. [h]$\mathbf{HL}^3$ = 2-formylpyridine-*para*-chloro-phenyl hydrazone. [i]$\mathbf{HL}^4$ = 2-pyridine-carboxaldehyde 4-dimethylaminobenzoylhydrazone. [j]$\mathbf{HL}^5$ = condensation product of 2-acetylpyridine and acetyl hydrazide. [k]$\mathbf{HL}^6$ = condensation product of 2-formylpyridine and acetyl hydrazide. [l]$\mathbf{L}^7$ = methyl 2-pyridyl ketone semicarbazone. [m]$\mathbf{L}^8$ = 2-benzoylpyridine-3-methoxybenzhydrazone. [n]$\mathbf{L}^9$ = condensation product of adamantane-1-carbohydrazide and 2-acetylpyridine. [o]$\mathbf{L}^{10}$ = condensation product of adamantane-1-carbohydrazide and di(2-pyridyl) ketone.

L and two bridging chlorine atoms (Cl1 and Cl1 at -*x*, -*y*, -*z*+1) (Figure 3). The Cu(II) ion in **3** adopts a distorted square pyramidal geometry with an index of trigonality (τ_5)[54] of 0.17 ($\tau_5 = (\beta - \alpha)/60$, where β and α are the two largest angles around the central atom; τ_5 is 0 for regular square based pyramidal geometry and 1.00 for regular trigonal bipyramidal geometry). The square base of the Cu(II) center is formed by pyridyl (N1) and imine (N2) nitrogen atoms and enolate oxygen (O1) of **L** and one chloride ion (Cl1), while the apical position is occupied by the symmetry related chloride ion at -*x*, -*y*, -*z*+1. The chloride ion bridges in an asymmetric (basal−apical) fashion so that the in-plane and axial Cu−Cl bond lengths are significantly different, Cu1−Cl1 = 2.2408(8) Å and Cu1−Cl1^{ii} = 2.6800(9)Å (where ii stands for -*x*, -*y*, -*z*+1). The asymmetric bridging mode of chlorido ligands has also been established in complexes **11**−**14** (Table 1). In **3** and **11**−**14**, the four-membered Cu_2Cl_2 bridging units are constrained to be planar by the presence of the symmetry element with the Cu···Cu separations ranging from 3.2926(5) to 3.4085(8) Å and Cu−Cl−Cu angles from 83.94(2)° to 88.33(3)°. Complexes **3** and **11** show the same degree of trigonal distortion of the regular square pyramidal geometry. For the other binuclear complexes listed in Table 1, the τ_5 value varies from 0.02 to 0.11, indicating that these structures are closer to the ideal square pyramidal configuration. The Cu(II) ions in **3** and **11**−**14** are displaced by the distance ρ of 0.1034(2)−0.2468(4) Å from the basal N, N, O, Cl plane toward the apical chlorine atom. In the crystal structure of complex **3**, the dimeric molecules self-assemble within the layer parallel with the (0 1 0) lattice plane by means of $\pi\cdots\pi$ stacking interactions between the adjacent aromatic rings of **L** and C−H···Cl hydrogen bonds. The BF_4^- anions, placed in between the adjacent layers, are involved in the intermolecular C−H···F hydrogen bonds and serve to connect the neighboring layers, as well as support stacking of the aromatic rings along the [100] (cf., SI).

3.3. DFT Calculations on Monomer Units. To investigate the nature of bonding of counter-anions in the structures of the complexes **1**−**4**, energy decomposition analysis has been performed, and the results are summarized in Table 2. Note that the inner sphere is taken from corresponding X-ray structures (**1**−**4**), and in this section, interaction with counter-anions is emphasized. In the case of **1**, the geometry of BF_4^- does not influence the analysis (Table S7 in Supporting Information summarizes the analysis on the

Table 2. Energy Decomposition Analysis of $[CuLCl]^+$--X^- in Monomer Structures 1, 2, 3, and 4 at Different Levels of Theory[a]

$[CuLCl]^+$--X^-	Energy Component	BP86-D3	PBE-D3	revPBE-D3	M06L-D3
1--BF_4^-	E_{elst}	−64.15	−64.57	−64.78	−63.72
	E_{Pauli}	13.00	10.86	14.16	5.34
	E_{orb}	−13.43	−13.43	−13.47	−14.74
	E_{disp}	−5.46	−3.22	−5.81	−0.79
	E_{int}	−70.04	−70.35	−69.91	−73.91
	Δq	0.08	0.07	0.07	0.07
2--NO_3^-	E_{elst}	−71.39	−71.73	−71.91	−71.15
	E_{Pauli}	16.34	14.23	17.89	7.44
	E_{orb}	−18.77	−18.98	−18.73	−18.39
	E_{disp}	−6.45	−3.84	−7.15	−0.77
	E_{int}	−80.27	−80.32	−79.89	−82.88
	Δq	0.25	0.21	0.20	0.14
3--BF_4^-	E_{elst}	−66.52	−66.59	−66.61	−66.25
	E_{Pauli}	4.47	2.52	4.38	0.42
	E_{orb}	−8.02	−8.14	−8.22	−8.47
	E_{disp}	−2.96	−1.9	−3.33	−0.66
	E_{int}	−73.7	−74.11	−73.77	−74.96
	Δq	0.03	0.03	0.03	0.02
4--ClO_4^-	E_{elst}	−62.16	−62.40	−62.56	−62.02
	E_{Pauli}	11.72	9.28	12.71	3.68
	E_{orb}	−12.78	−12.91	−12.81	−13.58
	E_{disp}	−7.89	−4.55	−8.20	−1.01
	E_{int}	−71.11	−70.58	−70.86	−72.93
	Δq	0.09	0.09	0.09	−0.08

[a]Energy components are given in kcal/mol; Δq is Hirshfeld charge, transferred between fragments; coordinates of all atoms are extracted from corresponding X-ray structures except in the case of **4** where O(perchlorate) atoms are optimized at the revPBE/def2-TZVP level of theory because of disorder in the X-ray structure.

structure with optimized F atoms). In the X-ray structure of **4**, the geometry of ClO_4^- deviates markedly from the expected tetrahedral shape. Optimization of O atoms recovers tetrahedral geometry of ClO_4^-. Consequently, there are some differences in energy components between the two considered structures, but general trends in the interactions in **4**−ClO_4^- are the same. In the following discussion, results of the **4**−ClO_4^- with optimized O(perchlorate) will be given, while the results on the structures where all atoms are

DOI: 10.1021/acs.cgd.9b00760
Cryst. Growth Des. 2019, 19, 4810−4821

extracted from the crystal structure of **4** are reported in the SI (Table S8, Figure S5 in Supporting Information).

In all the structures, the most dominant stabilizing term is electrostatic interaction between the fragments. It accounts for approximately 75−85% of the stabilization. Pauli repulsion is small, because of the large separation between the fragments. Dispersion correction is non-negligible (approximately 4−7% of the stabilization). The choice of density functional approximation is not affecting the results, with only small numerical differences. The only differences are present in the case of M06L-D3 because M06L in its parametrization already encompasses dispersion. Therefore, in this case, dispersion corrections are negligible. Consequently, Pauli repulsion in M06L-D3 is smaller than with standard GGA functionals.

The significance of the electrostatic stabilization is evident because of the charged fragments and is further illustrated in the electrostatic potential surfaces (Figure 4). The color code

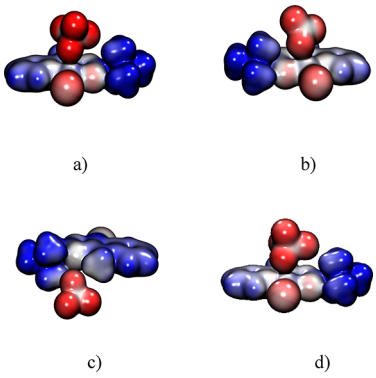

Figure 4. Electrostatic potential surfaces (at 0.01 au) from −0.13 (red) to +0.13 (blue) a.u. of monomeric units $[CuLCl]^+$--X^-: (a) **1**--BF_4^-, (b) **2**--NO_3^-, (c) **3**--BF_4^-, (d) **4**--ClO_4^-.

in Figure 4 is "Red-White-Blue". It ranges from deep red, indicating negatively charged regions, to deep blue, positively charged regions. The counter-anions carry most of the negative charge. Positive charge is delocalized in $[CuLCl]^+$ moiety. The most positive region is the $N(CH_3)_3$ group from the side chain of the **L**.

The preceding analysis shows clearly a prominent role of electrostatics in the interaction between $[CuLCl]^+$ and counter-anions. In the case of **1**, **3**, and **4** this is additionally confirmed with a small charge transfer, Δq in Table 2, between the fragments. However, in **2**, the charge transfer is non-negligible (Table 2). Furthermore, E_{orb}, that often indicates covalency,[55] in all four cases, contributes between 10% and 20% to the stabilization. Nevertheless, E_{orb} incorporates both the effects of covalency (charge transfer between the fragments) and polarization. To clarify the contribution of sole covalency, NOCV analysis has been performed. The most important density deformation channels related to the covalency are depicted in Figure 5. Two types of covalent interactions are found. The first one is metal−ligand covalency, i.e., ligand-to-metal charge transfer present in **1**, **2**, and **4**. The second type of covalent bonding is found in all structures and is a covalent part of the hydrogen bonding between the counter-anion and the $N(CH_3)_3$ group. In all the molecules, covalency is of minor importance, and polarization, i.e., electron density redistribution on one fragment due to the presence of another one is dominating to the E_{orb}.

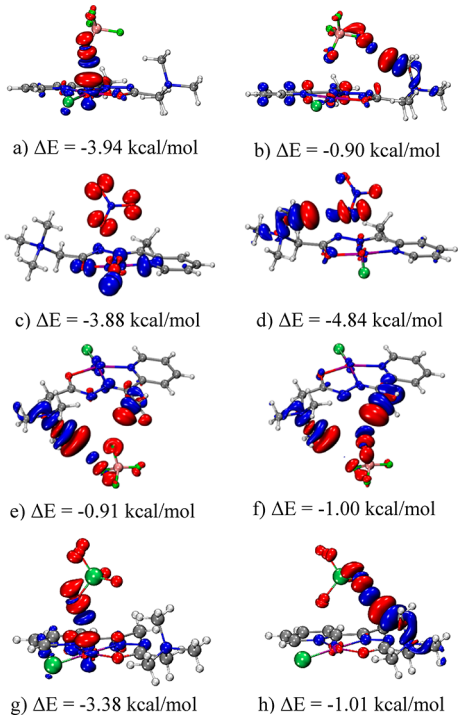

Figure 5. Most important covalent deformation density channels from NOCV analysis of $[CuLCl]^+$--X^- interaction: (a) **1**--BF_4^- metal−ligand (isovalue 0.001 a.u.), (b) **1**--BF_4^- hydrogen bond (isovalue 0.0003 a.u.), (c) **2**--NO_3^- metal−ligand (isovalue 0.001 a.u.), (d) **2**--NO_3^- hydrogen bond (isovalue 0.0003 a.u.), (e) and (f) **3**--BF_4^- hydrogen bond (isovalue 0.0002 a.u.), (g) **4**--ClO_4^- metal−ligand (isovalue 0.001 a.u.), (h) **4**--ClO_4^- hydrogen bond (isovalue 0.0003 a.u.). Red/blue color represent electron outflow/inflow.

Detailed noncovalent interactions present in these systems are shown in Figure 6. NCI plots show different interactions as

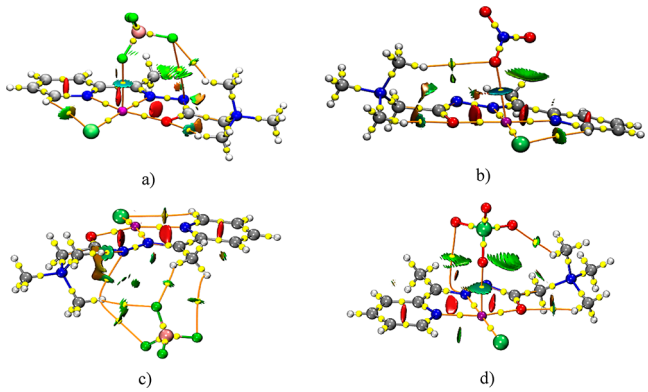

Figure 6. Three dimensional NCI plots for (a) **1**--BF_4^-, (b) **2**--NO_3^-, (c) **3**--BF_4^-, (d) **4**--ClO_4^-. Isosurfaces (isovalue $s = 0.4$) are colored in range $-0.03 < \text{sign}(\lambda_2) \times \rho < 0.02$ ("Blue-Green-Red" color scheme). Bond paths, connecting bond critical points (yellow spheres), and nuclear critical points (coinciding with atoms) are shown as orange lines.

distinctly colored and shaped regions. Strong attractive interactions are blue, weak attractive interactions and van der Waals interactions are green, and steric repulsion is red. Localized interactions are disk-shaped, while delocalized interactions are depicted as diffused surfaces. In all four molecules, interactions in $[CuLCl]^+$ fragments are identified:

DOI: 10.1021/acs.cgd.9b00760
Cryst. Growth Des. 2019, 19, 4810−4821

red disks in the middle of the two chelate rings, and the middle of the pyridine ring indicate ring-strain; weak intramolecular hydrogen bonds between Cl^- and pyridine CH, and between O1 and methyl group in $N(CH_3)_3$ group from the side chain of the L, are identified as small green disks. Electrostatic interactions between counter-anions and Cu(II) in **1**, **2**, and **4** are shown as blue-green disks. In **3**, BF_4^- and **L** are connected by hydrogen bonds (interactions between BF_4^- and $N(CH_3)_3$ and between $BF_4^-$and C7H). Hydrogen bonding between counter-anions and $N(CH_3)_3$ is present also in **1**, **2**, and **4**. In these three molecules, there are also van der Waals interactions between anions and chelate Cu−N−N−C−O rings.

Intermolecular interactions are also seen in IGM plots (Figure 7). In **1**, BF_4^- is bonded electrostatically with Cu(II),

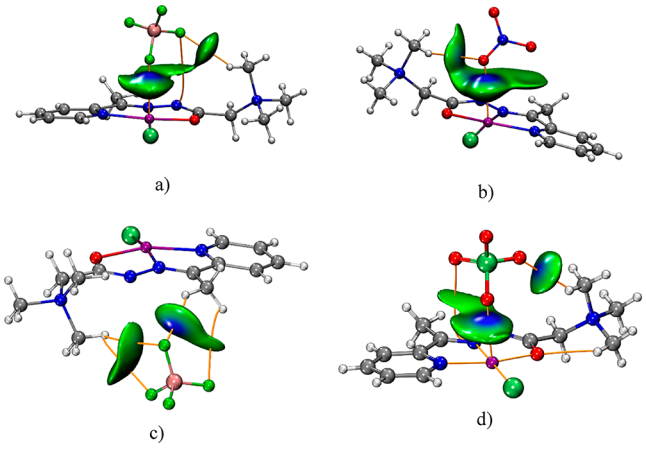

Figure 7. IGM plots for (a) **1**--BF_4^-, (b) **2**--NO_3^-, (c) **3**--BF_4^-, (d) **4**--ClO_4^-; isosurfaces of δg^{inter} (isovalue 0.004) colored by sign(λ_2) × ρ (range −0.05 to 0.05, "Blue-Green-Red" color scheme). Interfragment bond paths are shown as orange lines.

there is hydrogen bonding between BF_4^- and $N(CH_3)_3$ and van der Waals interaction between BF_4^- and N3 of the Cu−N−N−C−O chelate ring. In **2**, there are a strong electrostatic NO_3^-···Cu(II) interaction, hydrogen bonding between the NO_3^- and $N(CH_3)_3$ groups, and evident anion−π van der Waals interactions between NO_3^- and Cu−N−N−C−O chelate ring. The situation in **4** is equivalent. In **3**, there are two nonequivalent regions of hydrogen bonding between BF_4^- and $[CuLCl]^+$ fragments.

All the interactions are also identified in the framework of Bader's QTAIM method, with the presence of corresponding critical points and bond paths (Figures 6 and 7 and Figure S7 in Supporting Information). The topological properties of the electron density in the bond critical points (Table S9 in Supporting Information) confirms the ionic nature of bonding between counter-anions and Cu(II), as well as additional weak hydrogen bonding between counter-anions and $[CuLCl]^+$ fragments. IGM plots of δg^{inter} around Cu(II) ion in **1**, **2**, and **4** (Figure S6 in Supporting Information) show a distinction between metal−ligand in-plane bonds (Cu−N1, Cu−N2, Cu−O1, and Cu−Cl1) and Cu(II)−anion bonds. Metal−ligand in-plane bonds are typical coordination bonds, while bonding with anions is obviously weaker but definitively present.

All these results, taking into account both covalent and all noncovalent interactions, suggests that in structures **1**, **2**, and **4** anions are weakly coordinatively bound to Cu(II) with high ionic character, while in **3** hydrogen bonding is responsible for the position of the counter-anion.

3.4. DFT Study of Binuclear Complexes. As indicated before, regardless of reaction conditions (additional experimental details are in SI), only complex **3** has been obtained as a binuclear species. However, in **1**, **2**, and **4**, monomeric units in the crystal are placed in a way that two Cu(II) ions are on a somewhat shorter distance than if the units are completely separated. Therefore, we performed DFT calculations to analyze interactions between units in all four complexes.

Energy decomposition analysis of the formation of dimeric structures from monomer complexes is given in Table 3.

Table 3. Energy Decomposition Analysis of [CuLCl]--[CuLCl] Dimeric Structures of 1, 2, 3, and 4 at Different Levels of Theory[a]

[CuLClX]--[CuLClX]	Energy Component	BP86-D3	PBE-D3	revPBE-D3	M06L-D3
(BF_4^-)**1**--**1**(BF_4^-)	E_{elst}	−20.03	−20.55	−20.46	−18.07
	E_{Pauli}	32.34	28.67	35.04	13.64
	E_{orb}	−15.49	−15.55	−15.21	−18.21
	E_{disp}	−21.5	−12.11	−21.66	−2.93
	E_{int}	−24.67	−19.54	−22.29	−25.57
	Δq	0.00	0.00	0.00	0.00
(NO_3^-)**2**--**2**(NO_3^-)	E_{elst}	−9.34	−9.65	−9.69	−8.59
	E_{Pauli}	19.70	15.90	21.69	2.94
	E_{orb}	−11.24	−11.30	−11.12	−14.76
	E_{disp}	−20.77	−11.71	−20.63	−2.93
	E_{int}	−21.65	−16.76	−19.75	−23.34
	Δq	0.00	0.00	0.00	0.00
3	E_{elst}	−44.26	−44.43	−44.03	−42.02
	E_{Pauli}	56.91	54.49	59.91	41.63
	E_{orb}	−24.37	−24.36	−23.86	−26.71
	E_{disp}	−15.62	−8.53	−15.68	−1.88
	E_{int}	−27.34	−22.84	−23.66	−28.98
	Δq	0.00	0.00	0.00	0.00
(ClO_4^-)**4**--**4**(ClO_4^-)	E_{elst}	−21.78	−22.21	−22.11	−20.04
	E_{Pauli}	33.23	29.73	35.67	15.74
	E_{orb}	−16.19	−16.25	−15.92	−18.93
	E_{disp}	−20.49	−11.55	−20.50	−2.93
	E_{int}	−25.22	−20.28	−22.85	−26.16
	Δq	0.00	0.00	0.00	0.00

[a]Energy components are given in kcal/mol; Δq is Hirshfeld charge, transferred between fragments; coordinates of all atoms are extracted from corresponding X-ray structures except in the case of **4** where O(perchlorate) atoms are optimized at revPBE/def2-TZVP level of theory because of disorder in the X-ray structure.

Geometries of BF_4^- and ClO_4^- does not influence the analysis (Table S10 in Supporting Information summarizes the analysis on the structure **1**--**1** with optimized F atoms, and Table S11 of the analysis of the structure **4**--**4** with all atoms taken from the X-ray structure of **4**).

From first sight, one can see a prominent role of the dispersion in interaction energies. As in the case of monomers, different density functional approximations give consistent results. The only exception is M06L-D3, where a dispersion, contained in the functional form, clearly lowers E_{Pauli} while the D3 part is only a further correction to the energy. Electrostatic attraction is bringing two neutral monomers together in a parallel displaced manner (Figure S8 in Supporting Information). Covalency seems negligible in all four analyzed model

DOI: 10.1021/acs.cgd.9b00760
Cryst. Growth Des. 2019, 19, 4810−4821

binuclear structures, as the net charge transfer between two monomers, Δq, Table 3, is zero. NOCV analysis (Figure 8) establishes that only in **3**, the covalent σ bond between Cu−Cl^{ii} brings considerable stabilization (it brings around 12% of the stabilization).

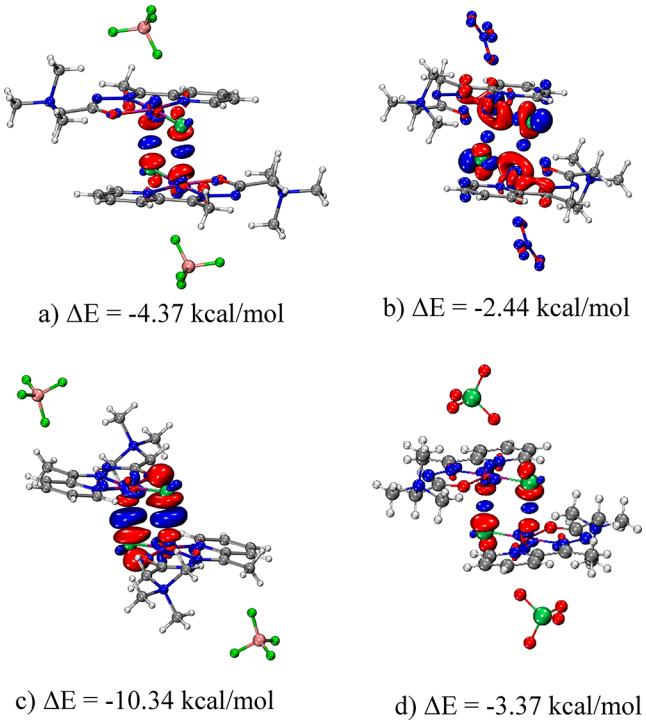

Figure 8. Most important covalent deformation density channels from NOCV analysis of [CuLClX]--[CuLClX] interactions: (a) **1--1** (isovalue 0.001 a.u.), (b) **2--2** (isovalue 0.0002 a.u.), (c) **3** (isovalue 0.001 a.u.), (d) **4--4** (isovalue 0.0008 a.u.). Red/blue color represents electron outflow/inflow.

To further understand the importance of dispersion, the interaction energies were also calculated with the ORCA program package using the revPBE-D3/ZORA-def2-TZVP level of theory, as well as the Grimme's fourth generation dispersion energy correction (revPBE-D4[56]) and the non-self-consistent and self-consistent nonlocal density-dependent dispersion functional (revPBE-NL and revPBE-SCNL,[43] respectively). In Table 4, the results at the revPBE/TZP level of theory from Table 3 are also summarized, where the E_{int} is given both relative to the quasi-restricted fragments (as done in the energy decomposition analysis, Table 3) and relative to the electronically fully relaxed unrestricted monomers. The difference is around 1 kcal/mol. All the results in Table 4 are consistent. revPBE results here are considered to be "dispersion-free".[57] We see that without dispersion, the interaction energy of two monomer units in the dimer of **2** are positive. In the case of dimers of **1** and **4**, interaction energies are close to zero or positive (in the range approximately from −2 to +1 kcal/mol). Only in the case of **3** is interaction energy, even without dispersion, negative.

Interestingly, in all four systems, interaction energies between monomers are similar (from −17 kcal/mol to −25 kcal/mol). However, the nature of the interactions is different. Energy decomposition analysis (Table 3), coupled with careful NOCV analysis (Figure 8) and comparison of dispersion-corrected with "dispersion-free" results (Table 4), allow estimation of various contributions to the interaction energies, namely, contribution of electrostatics, covalency, polarization, and dispersion. In the case of **3**, most of the stabilization comes from the electrostatics (53% of stabilization). Covalency brings around 12% of the stabilization, polarization approximately 16%, and dispersion around 18%. In the case of dimers of **1** and **4**, electrostatics and dispersion are of similar importance (both around 35% of the stabilization). Polarization contributes around 20% to the stabilization and covalency is of minor importance (around 5%). Dimer of **2** is mainly stabilized by dispersion interactions (50% of stabilization), electrostatics and polarization provide both around 22% of stabilization, and covalency is of minor importance (5% of stabilization).

Detailed noncovalent interactions between monomers are depicted in Figure 9 (NCI plots) and Figure 10 (IGM plots). Strong Cu−Cl^{ii} interactions are apparent in **3**—strong blue disks in the NCI plot and blue region in the IGM plot, together with orange-red area in the NCI plot, indicating strain in the formed Cu−Cl^{ii}−Cu^{ii}−Cl ring. These Cu−Cl^{i}

Table 4. Influence of Various Dispersion Corrections (Grimme's D3, Grimme's D4, Nonlocal Density-Dependent Non-Self-Consistent (NL) and Nonlocal Density-Dependent Self-Consistent (SCNL) Fuctionals) to the revPBE/ZORA-def2-TZVP Interaction Energies of [CuLClX]--[CuLClX] in Dimer Structures of 1, 2, 3, and 4[a]

CuLClX]--[CuLClX]	Energy	revPBE[b]	revPBE-D3[b]	revPBE-D4[b]	revPBE-NL[b]	revPBE-SCNL[b]	revPBE[c,d]	revPBE-D3[c,d]
1-1	E_{int}	0.28	−21.38	−21.13	−21.03	−21.50	−0.63 (0.74)	−22.29 (−20.92)
	E_{disp}	0.00	−21.66	−21.41	−21.32	−21.78	0.00	−21.66
1-1 (F-opt)[e]	E_{int}	0.13	−21.53	−21.25	−21.19	−21.66	−0.75 (0.64)	−22.41 (−21.02)
	E_{disp}	0.00	−21.66	−21.38	−21.32	−21.79	0.00	−21.66
2-2	E_{int}	2.23	−18.40	−17.57	−17.42	−17.89	0.88 (2.99)	−19.75 (−17.64)
	E_{disp}	0.00	−20.63	−19.80	−19.65	−20.12	0.00	−20.63
3	E_{int}	−8.15	−23.84	−25.50	−25.29	−25.58	−7.98 (−6.64)	−23.66 (−22.33)
	E_{disp}	0.00	−15.68	−17.35	−17.14	−17.43	0.00	−15.68
4-4	E_{int}	1.50	−19.00	−18.98	−18.73	−19.18	1.04 (2.24)	−19.47 (−18.06)
	E_{disp}	0.00	−20.50	−20.48	−20.32	−20.68	0.00	−20.50
4-4 (O-opt)[f]	E_{int}	−1.22	−21.72	−21.56	−21.32	−21.76	−2.35 (−0.67)	−22.85 (21.17)
	E_{disp}	0.00	−20.50	−20.34	−20.10	−20.34	0.00	−20.50

[a]Comparison with results of revPBE-D3/TZP results is also given. All the energies are given in kcal/mol. [b]Calculations with ORCA program package. [c]Calculations with ADF program package. [d]Results in brackets are relative to unrestricted monomers. [e]F atoms of BF_4^- optimized. [f]O atoms of ClO_4^- optimized.

DOI: 10.1021/acs.cgd.9b00760
Cryst. Growth Des. 2019, 19, 4810−4821

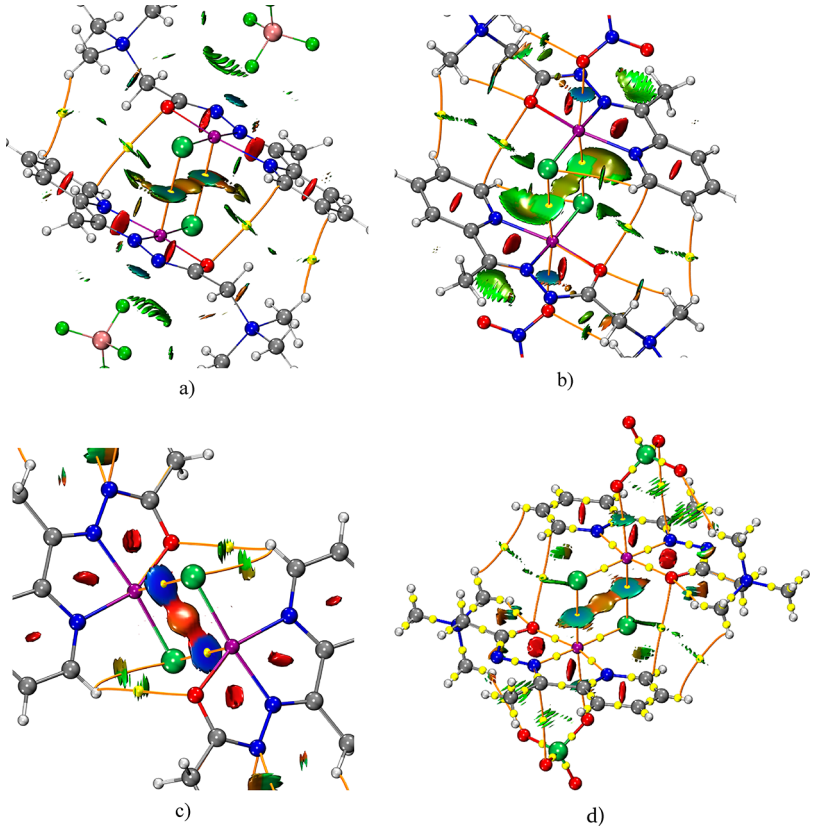

Figure 9. Three-dimensional NCI plots for (a) **1**--**1**, (b) **2**--**2**, (c) **3**, and (d) **4**--**4**. Isosurfaces (isovalue $s = 0.4$) are colored in the range $-0.03 < \text{sign}(\lambda 2)\ \rho < 0.02$ ("Blue-Green-Red" color scheme). Interfragment bond paths, connecting bond critical points (yellow spheres), and nuclear critical (coinciding with atoms) points are shown as orange lines.

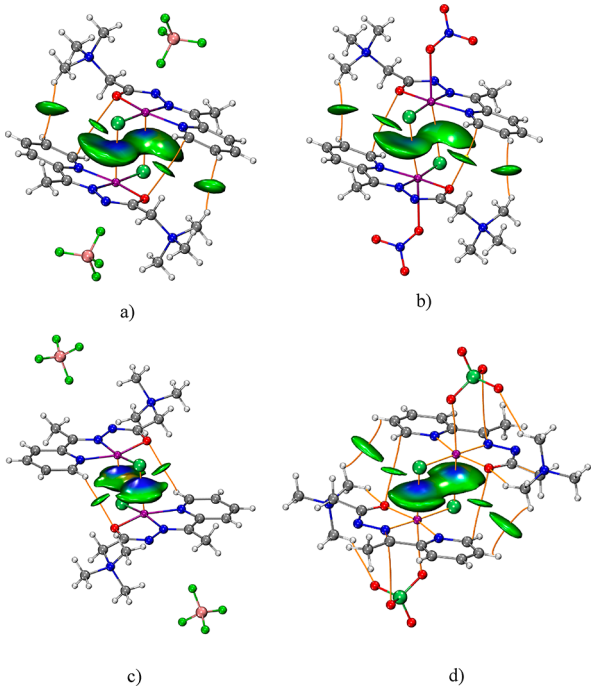

Figure 10. Isosurfaces of δg^{inter} (isovalue 0.004) colored by $\text{sign}(\lambda 2) \times \rho$ (range −0.05 to 0.05, "Blue-Green-Red" color scheme) for (a) **1**--**1**, (b) **2**--**2**, (c) **3**, (d) **4**--**4**. Interfragment bond paths are shown as orange lines.

interactions are weaker in **1** and **4**, revealed in NCI and IGM plots by greener color. In **2**, Cu−Cl^{i} interactions are of the van der Waals type (diffuse green surface). IGM plots showing only interactions around Cu(II) (Figure S9 in Supporting Information), revealing that in **3** Cl^{-} acts as a bridging ligand, and confirms that in **2** Cu−Cl^{i} interactions are of the van der Waals type. Cu−Cl^{i} interactions in **1** and **4** are in between these two. Additional attractive interactions are found in all four dimers. Two types of van der Waals interactions are encountered. The first one is between pyridine on one monomer and the $N(CH_3)_3$ group on the other monomer. The second is between pyridine and O1. Topological properties of the electron density (Figure S10, Table S12 in Supporting Information) additionally confirm these types of interactions between monomer units.

Results of the energy decomposition analysis and analysis of the noncovalent interactions assert that only **3** has a clear dimer structure, in accordance with experimental findings. In the other three cases, two monomers mainly interact via van der Waals attractive forces, explaining the shortest Cu−Cu contact in **3**.

4. CONCLUSIONS

The complexes $[CuLCl]BF_4$, $[CuLCl]NO_3$, and $[Cu_2L_2Cl_2](BF_4)_2$ have been synthesized and characterized by X-ray crystallographic analysis. The structures of $[CuLCl]BF_4$ and $[CuLCl]NO_3$ are analogous to the previously reported $[CuLCl]ClO_4$. Geometries around Cu(II) ions in the mononuclear complexes can be described either as distorted square planar or as distorted square pyramidal. Coordination

DOI: 10.1021/acs.cgd.9b00760
Cryst. Growth Des. 2019, 19, 4810−4821

around Cu(II) depends on the nature of bonding of BF_4^-, NO_3^-, and ClO_4^- to the Cu(II) ion. In other words, coordination geometry will depend on whether the BF_4^-, NO_3^-, and ClO_4^- are considered as counter-anions or ligands. DFT calculations revealed that in all three mononuclear complexes, they are weakly coordinatively bound to Cu(II), with high ionic character. Hence, their structural formulas could also be written as [Cu**L**ClBF_4], [Cu**L**ClNO_3], and [Cu**L**ClClO_4]. It is noteworthy to mention that these ligands are weakly bonded, and in solution, they might dissociate, hence, e.g., conductivity measurements in solution will not give an accurate picture of what the structures would be in crystals. In binuclear $[Cu_2L_2Cl_2](BF_4)_2$, BF_4^- is clearly a counter-anion, and its position is a consequence of hydrogen bonding with **L**. In accordance with the experimental findings, DFT calculations establish that only complex **3** exists as a binuclear species, where two Cu(II) ions are connected via bridging Cl^- ions. Complexes **1**, **2**, and **4** form structures where units are held together via attractive van der Waals forces.

The present study shows that ambiguity about the actual coordination number in the real crystal structures of coordination compounds can be overcome with the aid of DFT based calculations, like analysis of interaction energy components, NCI and IGM plots, and QTAIM analysis.

■ ASSOCIATED CONTENT

Supporting Information

The Supporting Information is available free of charge on the ACS Publications website at DOI: 10.1021/acs.cgd.9b00760.

X-ray crystallography; Additional experimental details for the synthesis of **1** and **3**; Additional computational results for mononuclear structures; Additional computational results for dimer structures (PDF)

Accession Codes

CCDC 1917721−1917723 contain the supplementary crystallographic data for this paper. These data can be obtained free of charge via www.ccdc.cam.ac.uk/data_request/cif, or by emailing data_request@ccdc.cam.ac.uk, or by contacting The Cambridge Crystallographic Data Centre, 12 Union Road, Cambridge CB2 1EZ, UK; fax: +44 1223 336033.

■ AUTHOR INFORMATION

Corresponding Authors

*E-mail: radanovic@chem.bg.ac.rs.

*E-mail: matijaz@chem.bg.ac.rs.

ORCID

Božidar Čobeljić: 0000-0001-6335-0196

Maja Gruden: 0000-0002-0746-5754

Andrej Pevec: 0000-0001-7008-608X

Matija Zlatar: 0000-0002-3809-0940

Author Contributions

The manuscript was written through the contributions of all authors. All authors have given approval to the final version of the manuscript.

Notes

The authors declare no competing financial interest.

■ ACKNOWLEDGMENTS

This work was supported by the Ministry of Education, Science and Technological Development of the Republic of Serbia (Grants OI 172035 and OI 172055) and the Slovenian Research Agency (P-0175).

■ REFERENCES

(1) Díaz-Torres, R.; Alvarez, S. Coordinating ability of anions and solvents towards transition metals and lanthanides. *Dalt. Trans.* **2011**, *40* (40), 10742.

(2) Rosenthal, M. R. The myth of the non-coordinating anion. *J. Chem. Educ.* **1973**, *50* (5), 331.

(3) Halcrow, M. A. Jahn−Teller distortions in transition metal compounds, and their importance in functional molecular and inorganic materials. *Chem. Soc. Rev.* **2013**, *42* (4), 1784−1795.

(4) Gruden-Pavlović, M.; Zlatar, M.; Schläpfer, C.-W.; Daul, C. DFT study of the Jahn−Teller effect in Cu(II) chelate complexes. *J. Mol. Struct.: THEOCHEM* **2010**, *954* (1−3), 80−85.

(5) Milenković, M. R.; Papastavrou, A. T.; Radanović, D.; Pevec, A.; Jagličić, Z.; Zlatar, M.; Gruden, M.; Vougioukalakis, G. C.; Turel, I.; Anđelković, K.; et al. Highly-efficient N-arylation of imidazole catalyzed by Cu(II) complexes with quaternary ammonium-functionalized 2-acetylpyridine acylhydrazone. *Polyhedron* **2019**, *165*, 22−30.

(6) Ziegler, T.; Rauk, A. On the calculation of bonding energies by the Hartree Fock Slater method. *Theor. Chim. Acta* **1977**, *46* (1), 1−10.

(7) Ziegler, T.; Rauk, A. A theoretical study of the ethylene-metal bond in complexes between copper(1+), silver(1+), gold(1+), platinum(0) or platinum(2+) and ethylene, based on the Hartree-Fock-Slater transition-state method. *Inorg. Chem.* **1979**, *18* (6), 1558−1565.

(8) Bickelhaupt, F. M.; Baerends, E. J.; Lipkowitz, K. B.; Boyd, D. B. Kohn-Sham Density Functional Theory: Predicting and Understanding Chemistry. *Reviews in computational chemistry* **2007**, *15*, 1−86.

(9) Johnson, E. R.; Keinan, S.; Mori-Sánchez, P.; Contreras-García, J.; Cohen, A. J.; Yang, W. Revealing Noncovalent Interactions. *J. Am. Chem. Soc.* **2010**, *132* (18), 6498−6506.

(10) Lefebvre, C.; Rubez, G.; Khartabil, H.; Boisson, J.-C.; Contreras-García, J.; Hénon, E. Accurately extracting the signature of intermolecular interactions present in the NCI plot of the reduced density gradient versus electron density. *Phys. Chem. Chem. Phys.* **2017**, *19* (27), 17928−17936.

(11) Lefebvre, C.; Khartabil, H.; Boisson, J.-C.; Contreras-García, J.; Piquemal, J.-P.; Hénon, E. The Independent Gradient Model: A New Approach for Probing Strong and Weak Interactions in Molecules from Wave Function Calculations. *ChemPhysChem* **2018**, *19* (6), 724−735.

(12) Bader, R. F. W. A quantum theory of molecular structure and its applications. *Chem. Rev.* **1991**, *91* (5), 893−928.

(13) *CrysAlis PRO*; Oxford Diffraction Ltd., Yarnton, England; https://www.rigaku.com/en/products/smc/crysalis (accessed May 15, 2019).

(14) Altomare, A.; Cascarano, G.; Giacovazzo, C.; Guagliardi, A. IUCr. Completion and refinement of crystal structures with SIR 92. *J. Appl. Crystallogr.* **1993**, *26* (3), 343−350.

(15) Sheldrick, G. M. IUCr. A short history of SHELX. *Acta Crystallogr., Sect. A: Found. Crystallogr.* **2008**, *64* (1), 112−122.

(16) Sheldrick, G. M. IUCr. Crystal structure refinement with SHELXL. *Acta Crystallogr., Sect. C: Struct. Chem.* **2015**, *71* (1), 3−8.

(17) Farrugia, L. J. IUCr. WinGX and ORTEP for Windows: an update. *J. Appl. Crystallogr.* **2012**, *45* (4), 849−854.

(18) Macrae, C. F.; Edgington, P. R.; McCabe, P.; Pidcock, E.; Shields, G. P.; Taylor, R.; Towler, M.; van de Streek, J. IUCr. Mercury: visualization and analysis of crystal structures. *J. Appl. Crystallogr.* **2006**, *39* (3), 453−457.

(19) Neese, F. The ORCA program system. *Wiley Interdiscip. Rev. Comput. Mol. Sci.* **2012**, *2* (1), 73−78.

(20) Neese, F. Software update: the ORCA program system, version 4.0. *Wiley Interdiscip. Rev. Comput. Mol. Sci.* **2018**, *8* (1), No. e1327.

(21) Zhang, Y.; Yang, W. Comment on "Generalized Gradient Approximation Made Simple. *Phys. Rev. Lett.* **1998**, *80* (4), 890−890.

DOI: 10.1021/acs.cgd.9b00760
Cryst. Growth Des. 2019, 19, 4810−4821

(22) Grimme, S.; Antony, J.; Ehrlich, S.; Krieg, H. A consistent and accurate ab initio parametrization of density functional dispersion correction (DFT-D) for the 94 elements H-Pu. *J. Chem. Phys.* **2010**, *132* (15), 154104.
(23) Grimme, S.; Ehrlich, S.; Goerigk, L. Effect of the damping function in dispersion corrected density functional theory. *J. Comput. Chem.* **2011**, *32* (7), 1456−1465.
(24) van Lenthe, E.; Baerends, E. J.; Snijders, J. G. Relativistic regular two-component Hamiltonians. *J. Chem. Phys.* **1993**, *99* (6), 4597−4610.
(25) van Lenthe, E.; Baerends, E. J.; Snijders, J. G. Relativistic total energy using regular approximations. *J. Chem. Phys.* **1994**, *101* (11), 9783−9792.
(26) van Wüllen, C. Molecular density functional calculations in the regular relativistic approximation: Method, application to coinage metal diatomics, hydrides, fluorides and chlorides, and comparison with first-order relativistic calculations. *J. Chem. Phys.* **1998**, *109* (2), 392−399.
(27) Pantazis, D. A.; Chen, X.-Y.; Landis, C. R.; Neese, F. All-Electron Scalar Relativistic Basis Sets for Third-Row Transition Metal Atoms. *J. Chem. Theory Comput.* **2008**, *4* (6), 908−919.
(28) Pantazis, D. A.; Neese, F. All-Electron Scalar Relativistic Basis Sets for the Lanthanides. *J. Chem. Theory Comput.* **2009**, *5* (9), 2229−2238.
(29) Weigend, F. Accurate Coulomb-fitting basis sets for H to Rn. *Phys. Chem. Chem. Phys.* **2006**, *8* (9), 1057−1065.
(30) Baerends, E. J.; Ziegler, T.; Atkins, A. J.; Autschbach, J.; Bashford, D.; Baseggio, O.; Bérces, A.; Bickelhaupt, F. M.; Bo, C.; Boerritger, P. M.; et al. *ADF2017, SCM, Theoretical Chemistry*; Vrije Universiteit, Amsterdam; The Netherlands; https://www.scm.com.
(31) Fonseca Guerra, C.; Snijders, J. G.; te Velde, G.; Baerends, E. J. Towards an order- N DFT method. *Theor. Chem. Acc.* **1998**, *99* (6), 391−403.
(32) te Velde, G.; Bickelhaupt, F. M.; van Gisbergen, S. J. A.; Fonseca Guerra, C. F.; Baerends, E. J.; Snijders, J. G.; Ziegler, T.; et al. Chemistry with ADF. *J. Comput. Chem.* **2001**, *22* (9), 931−967.
(33) Nalewajski, R. F.; Mrozek, J.; Mazur, G. Quantum chemical valence indices from the one-determinantal difference approach. *Can. J. Chem.* **1996**, *74* (6), 1121−1130.
(34) Mitoraj, M. P.; Michalak, A.; Ziegler, T. A Combined Charge and Energy Decomposition Scheme for Bond Analysis. *J. Chem. Theory Comput.* **2009**, *5* (4), 962−975.
(35) Hirshfeld, F. L. Bonded-atom fragments for describing molecular charge densities. *Theor. Chim. Acta* **1977**, *44* (2), 129−138.
(36) Becke, A. D. Density-functional exchange-energy approximation with correct asymptotic behavior. *Phys. Rev. A: At., Mol., Opt. Phys.* **1988**, *38* (6), 3098−3100.
(37) Perdew, J. P. Density-functional approximation for the correlation energy of the inhomogeneous electron gas. *Phys. Rev. B: Condens. Matter Mater. Phys.* **1986**, *33* (12), 8822−8824.
(38) Perdew, J.; Erratum, P. Density-functional approximation for the correlation energy of the inhomogeneous electron gas. *Phys. Rev. B: Condens. Matter Mater. Phys.* **1986**, *34* (10), 7406−7406.
(39) Perdew, J. P.; Burke, K.; Ernzerhof, M. Generalized Gradient Approximation Made Simple. *Phys. Rev. Lett.* **1996**, *77* (18), 3865−3868.
(40) Zhao, Y.; Truhlar, D. G. A new local density functional for main-group thermochemistry, transition metal bonding, thermochemical kinetics, and noncovalent interactions. *J. Chem. Phys.* **2006**, *125* (19), 194101.
(41) Zhao, Y.; Truhlar, D. G. The M06 suite of density functionals for main group thermochemistry, thermochemical kinetics, noncovalent interactions, excited states, and transition elements: two new functionals and systematic testing of four M06-class functionals and 12 other function. *Theor. Chem. Acc.* **2008**, *120* (1−3), 215−241.
(42) Lu, T.; Chen, F. Multiwfn: A multifunctional wavefunction analyzer. *J. Comput. Chem.* **2012**, *33* (5), 580−592.
(43) Hujo, W.; Grimme, S. Performance of the van der Waals Density Functional VV10 and (hybrid)GGA Variants for Thermochemistry and Noncovalent Interactions. *J. Chem. Theory Comput.* **2011**, *7* (12), 3866−3871.
(44) Vydrov, O. A.; Van Voorhis, T. Nonlocal van der Waals density functional: the simpler the better. *J. Chem. Phys.* **2010**, *133* (24), 244103.
(45) Chumakov, Y. M.; Tsapkov, V. I.; Antosyak, B. Y.; Bairac, N. N.; Simonov, Y. A.; Bocelli, G.; Pahontu, E.; Gulea, A. P. Crystal structures of copper(II) nitrate, copper(II) chloride, and copper(II) perchlorate complexes with 2-formylpyridine semicarbazone. *Crystallogr. Rep.* **2009**, *54* (3), 455−463.
(46) Sangeetha, N. R.; Pal, S.; Anson, C. E.; Powell, A. K.; Pal, S. A one-dimensional assembly of copper(II) polyhedra via dual use of hydrogen-bonding and $\pi-\pi$ interaction. *Inorg. Chem. Commun.* **2000**, *3* (8), 415−419.
(47) Despaigne, A. A. R.; da Silva, J. G.; Carmo, A. C. M. do; Sives, F.; Piro, O. E.; Castellano, E. E.; Beraldo, H. Copper(II) and zinc(II) complexes with 2-formylpyridine-derived hydrazones. *Polyhedron* **2009**, *28* (17), 3797−3803.
(48) Datta, A.; Das, K.; Jhou, Y.-M.; Huang, J.-H.; Lee, H. M. IUCr. Dichlorido{ N ′-[1-(2-pyridin-2-yl)ethylidene]acetohydrazide-κ 2 N ′, O }copper(II). *Acta Crystallogr., Sect. E: Struct. Rep. Online* **2011**, *67* (1), m123−m123.
(49) Datta, A.; Sheu, S.-C.; Liu, P.-H.; Huang, J.-H. IUCr. Dichlorido{ N ′-[(pyridin-2-yl)methylidene-κ N]acetohydrazide-κ 2 N ′, O }copper(II). *Acta Crystallogr., Sect. E: Struct. Rep. Online* **2011**, *67* (12), m1852−m1852.
(50) Shaabani, B.; Khandar, A. A.; Mahmoudi, F.; Maestro, M. A.; Balula, S. S.; Cunha-Silva, L. Novel binuclear Cu(II) complexes combining a semicarbazone Schiff base with distinct bridging ligands: Structure and antimicrobial activity. *Polyhedron* **2013**, *57*, 118−126.
(51) Fousiamol, M. M.; Sithambaresan, M.; Smolenski, V. A.; Jasinski, J. P.; Kurup, M. R. P. Halogen/azide bridged box dimer copper(II) complexes of 2-benzoylpyridine-3-methoxybenzhydrazone: Structural and spectral studies. *Polyhedron* **2018**, *141*, 60−68.
(52) Leovac, V. M.; Rodić, M. V.; Jovanović, L. S.; Joksović, M. D.; Stanojković, T.; Vujčić, M.; Sladić, D.; Marković, V.; Vojinović-Ješić, L. S. Transition Metal Complexes with 1-Adamantoyl Hydrazones - Cytotoxic Copper(II) Complexes of Tri- and Tetradentate Pyridine Chelators Containing an Adamantane Ring System. *Eur. J. Inorg. Chem.* **2015**, *2015* (5), 882−895.
(53) Yang, L.; Powell, D. R.; Houser, R. P. Structural variation in copper(i) complexes with pyridylmethylamide ligands: structural analysis with a new four-coordinate geometry index, τ 4. *Dalt. Trans.* **2007**, No. 9, 955−964.
(54) Addison, A. W.; Rao, T. N.; Reedijk, J.; van Rijn, J.; Verschoor, G. C. Synthesis, structure, and spectroscopic properties of copper(II) compounds containing nitrogen−sulphur donor ligands; the crystal and molecular structure of aqua[1,7-bis(N-methylbenzimidazol-2′-yl)-2,6-dithiaheptane]copper(II) perchlorate. *J. Chem. Soc., Dalton Trans.* **1984**, No. 7, 1349−1356.
(55) Zlatar, M.; Allan, M.; Fedor, J. Excited states of Pt(PF < inf > 3</inf>)<inf > 4</inf > and their role in focused electron beam nanofabrication. *J. Phys. Chem. C* **2016**, *120* (19), 10667−10674.
(56) Caldeweyher, E.; Bannwarth, C.; Grimme, S. Extension of the D3 dispersion coefficient model. *J. Chem. Phys.* **2017**, *147* (3), No. 034112.
(57) Horn, P. R.; Mao, Y.; Head-Gordon, M. Defining the contributions of permanent electrostatics, Pauli repulsion, and dispersion in density functional theory calculations of intermolecular interaction energies. *J. Chem. Phys.* **2016**, *144* (11), 114107.

DOI: 10.1021/acs.cgd.9b00760
Cryst. Growth Des. 2019, 19, 4810−4821